INTERNATIONAL JOURNAL FOR NUMERICAL METHODS IN FLUIDS
Int. J. Numer. Meth. Fluids 2004; **45**:1291–1315 (DOI: 10.1002/fld.739)

Prediction of unsteady, separated boundary layer over a blunt body for laminar, turbulent, and transitional flow

D. Scott Holloway*,†, D. Keith Walters‡ and James H. Leylek

Advanced Computational Research Laboratory, Department of Mechanical Engineering, Clemson University, Clemson, SC 29634, U.S.A.

SUMMARY

The focus of this paper is to study the ability of unsteady RANS-based CFD to predict separation over a blunt body for a wide range of Reynolds numbers particularly the ability to capture laminar-to-turbulent transition. A perfect test case to demonstrate this point is the cylinder-in-crossflow for which a comparison between experimental results from the open literature and a series of unsteady simulations is made. Reynolds number based on cylinder diameter is varied from 10^4 to 10^7 (subcritical through supercritical flow). Two methods are used to account for the turbulence in the simulations: currently available eddy–viscosity models, including standard and realizable forms of the k–ε model; and a newly developed eddy–viscosity model capable of resolving boundary layer transition, which is absolutely necessary for the type and range of flow under consideration. The new model does not require user input or 'empirical' fixes to force transition. For the first time in the open literature, three distinct flow regimes and the drag crisis due to the downstream shift of the separation point are predicted using an eddy–viscosity based model with transition effects. Discrepancies between experimental and computational results are discussed, and difficulties for CFD prediction are highlighted. Copyright © 2004 John Wiley & Sons, Ltd.

KEY WORDS: separation; laminar; transition; turbulent; cylinder-in-crossflow; unsteady RANS

1. INTRODUCTION

The state of the boundary layer in a region of separation plays an important role in the aerodynamics and heat transfer of many devices particularly blunt bodies. At engineering-level Reynolds numbers (Re_D), the drag over a blunt body is mostly contributed to form drag. If the boundary layer is turbulent, the flow will separate further downstream than if it is laminar. This leads to lower form and total drag for turbulent flow. To predict this type of flow using unsteady RANS, it is essential that the turbulence model be able to capture

*Correspondence to: D. Scott Holloway, Advanced Computational Research Laboratory, Department of Mechanical Engineering, Clemson University, Clemson, SC 29634, U.S.A.
†E-mail: dshollo@ces.clemson.edu
‡Currently at Mississippi State University.

Published online 25 May 2004

Received 25 November 2003
Revised 30 March 2004

both laminar, turbulent, and transitional boundary layers. A perfect test case to demonstrate this point is the cylinder-in-crossflow. Though the problem is simple in terms of geometry, currently available eddy–viscosity models are incapable of predicting the physics for this flow over a wide range of Re_D.

1.1. Background and description of flow

A schematic of the geometry and nomenclature of flow over a circular cylinder is shown in Figure 1. The physical phenomena encountered (unsteady wake, transition, etc.) in the cylinder-in-crossflow (CCF) are found in many industrial and scientific applications. The details of the flow regime (e.g. laminar vs turbulent, steady vs unsteady, location of separation) depend primarily on the Reynolds number (Re_D). Schlichting and Klaus [1] provides a description of flow regimes at various Re_D. For $Re_D < 40$, the entire flow is laminar and steady with attached counter-rotating vortices on the downstream half of the cylinder. For $40 < Re_D < 300$, the flow remains laminar, and an unsteady Karman vortex street is observed downstream of the cylinder. In the subcritical range ($300 < Re_D < 1–1.3\times10^5$), the boundary layer is laminar and separates at approximately 80°, and the downstream wake exhibits a turbulent, unsteady behaviour. The onset of turbulence in the separated shear layer moves towards the cylinder with increasing Re_D [2]. At a critical Reynolds number, there is significant decrease in drag due to a dramatic change in the nature of the boundary layer. In this regime, the laminar boundary layer separates, transitions to turbulence, reattaches, separates again, and produces a turbulent wake [1]. The behaviour of the transition is three-dimensional [3]. The value of the critical Re_D is sensitive to the freestream turbulence level and surface roughness. For quiescent flow over a smooth cylinder, the critical regime extends over $1.3\times10^5 < Re_D < 3.5\times10^6$. In the supercritical regime, the boundary layer transitions to turbulence on the cylinder surface and separates downstream at approximately 120°. Additional qualitative discussion can be found in Reference [4].

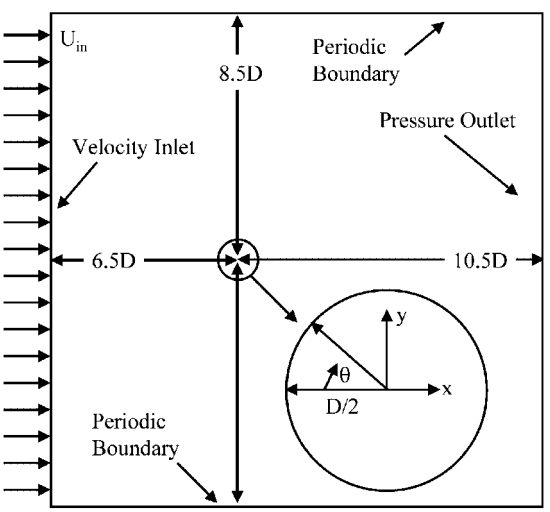

Figure 1. Schematic of geometry and computational domain used in this study.

1.2. Literature review

The open literature contains numerous experimental and numerical investigations of the CCF. Computational efforts have primarily involved the use of direct numerical simulations (DNS) or large eddy simulations (LES) at relatively low Reynolds number. There are, however, a handful of studies using LES and Reynolds-averaged Navier–Stokes (RANS) based simulations at the types of Re_D presently under consideration. The discussion concentrates on phenomena encountered for different flow regimes, drag coefficients, separation location, and the predictive capability of eddy–viscosity based turbulence models.

1.2.1. Experimental studies. Achenbach [5] examined a range of Re_D (6×10^4–5×10^6). Pressure and shear stress distribution along the cylinder, separation angle, and drag coefficient were presented. The mainstream turbulence level was 0.7%. The length to diameter ratio of the cylinder was relatively small (3.33), but measurements were taken at the centre of the cylinder to mitigate the wall blockage effects. For a subcritical $Re_D = 10^5$, the laminar boundary layer separated 78° downstream of the stagnation point. For a critical $Re_D = 8.5\times10^5$, the laminar boundary layer separated at 105°, transitioned to turbulence, reattached, and separated again at 147°. The location of both separations is inconsistent in the literature [5, 6]. At a supercritical $Re_D = 3.6\times10^6$, Achenbach found that the attached boundary layer transitioned on the surface and separated at 115°. Drag information was reported, but Roshko [7] showed that C_D for supercritical flow is very sensitive to experimental conditions.

1.2.2. Computational studies. Breuer [8] presented 3-D LES simulations of the CCF in the subcritical regime ($Re_D = 1.4\times10^5$). The finest mesh size was $325\times325\times64$ (325 cells around the circumference of the cylinder). The study implemented several subgrid models to compare with a benchmark experimental case [9]. Breuer found discrepancies in the predicted drag coefficient for the different subgrid models. The simulations showed separation to occur at 94°, which is downstream of the 'standard' value of 80°.

Selvam [10] performed a series of 2-D LES simulations for $10^4 < Re_D < 10^6$. A finite element approach was used with a 2260 cell mesh. Discrepancies between computational and experimental drag coefficients were attributed to the 2-D nature of the computations. Since no details were given about the flowfield, it is difficult to draw conclusions regarding the ability to predict the three distinct flow regimes.

Tamura *et al.* [11] studied flows ($10^3 < Re_D < 10^6$) using a technique called the third-order upwind scheme. The method accounts for turbulence through the discretization scheme. In contrast, the current work uses an eddy–viscosity based turbulence model. The study attempts to show the effects of using 2-D vs 3-D simulations. For 2-D, results change greatly when the mesh is changed from 100×100 to 800×100 cells. The authors conclude that drag coefficient can only be correctly predicted using 3-D simulations. However, several important physical mechanisms and numerical issues are not addressed. Transition, separation, grid-independence, and wake resolution are expected to be as important as the 3-D nature of the flow.

RANS-based simulations have shown little success in predicting flow over a blunt body at high Reynolds numbers. This is due to the inability of currently available turbulence models to resolve the effects of transition. These models are strictly applicable to fully turbulent flowfields, a condition only approximated for the supercritical regime, and only exactly satisfied

as $Re_D \to \infty$. Reichel and Strohmeier [12] demonstrated the ability of eddy–viscosity models (standard k–ε or SKE, realizable k–ε or RKE) and LES to predict the drag coefficient for Re_D ranging from 10^2 to 10^7. The grid consisted of 40 cells around the circumference of the cylinder. For SKE, the drag was found to exponentially decrease with an increase in Re_D. The study included a band of collected experimental data from the literature, and concluded that predicted values fall within a close enough range of the band to justify the use of fully turbulent models. It is difficult to judge the validity of the predictions without an examination of transition, separation, etc. in each flow regime.

Catalano *et al.* [13] compared 2-D results for LES and SKE using wall functions at critical and supercritical Reynolds numbers. For SKE, C_D varied little in time and was under-predicted at high Re_D. The low value of C_D was blamed on grid resolution and the absence of transitional effects in the turbulence model. The authors also found little sensitivity of the drag coefficient to Re_D in the critical regime and were unable to capture the separation bubble that has been seen experimentally for this case.

A typical method for including transitional effects is to artificially trip turbulence. Celik and Shaffer [14] used SKE and 2-D steady simulations to study flows ($10^4 < Re_D < 10^7$) on a mesh of 100×150 cells. The study implemented an empirical *a priori* method of fixing the transition point. For $Re_D = 3.6 \times 10^6$, the results showed that the flow separated at 118°. Travin *et al.* [15] applied the Detached eddy simulation technique to the 3-D cylinder-in-crossflow. For $Re_D = 5 \times 10^4$, a laminar separation was forced. For $Re_D = 1.4 \times 10^5$ and 3×10^6, a turbulent separation was forced. The artificial nature of the transition and the inability to obtain a grid-independent solution were two shortcomings of the work.

Saghafian *et al.* [16] performed a series of 2-D unsteady simulations of flow past a circular cylinder for Reynolds numbers ranging from 2×10^3 to 8.4×10^6. The mesh consisted of 16 800 cells. The authors employed both linear and non-linear eddy–viscosity models. Results from the linear model showed no transition, and consequently, an approximately constant relationship between drag coefficient and Reynolds number was obtained. When the non-linear, cubic eddy–viscosity model of Craft *et al.* [17] was employed, a transition was captured and the drag crisis was predicted. However, the model was unable to predict the separation bubble present in critical flow [5] and the drag coefficients for supercritical flows were over-predicted. The over-prediction of drag coefficient is interesting since the model also over-predicted the separation angle by several degrees. Over-prediction of the separation point should lead to a decrease in the predicted drag since a later separation leads to more pressure recovery. However, by examining the predicted static pressure distribution around the circumference of the cylinder, one can see that the over-prediction of drag coefficient was due to an unusual and significant decrease in static pressure between 165 and 180°. The authors attribute this to the 2-D nature of the simulations. However, this phenomenon is only seen at Reynolds numbers greater than 10^5.

Edwards *et al.* [18] performed a series of 2-D unsteady simulations of flow past a heated cylinder for Reynolds numbers ranging from 1.27×10^6 to 4×10^6. The geometry consisted of a half cylinder with centreline symmetry, and the mesh consisted of up to 100 000 cells. The authors developed a 1-equation transition model based on the Spalart–Allmaras turbulence model [19] and the work of Warren and Hassan [20, 21]. Unlike the model used in the present study, their model required input of boundary layer quantities to evaluate certain model terms. Since all of the test cases were for supercritical flow, transition occurred on the surface of the cylinder. Prediction of the point of transition was good, but heat transfer was

over-predicted. Critical and subcritical test cases were not considered due to their inability to predict separation-induced transition.

2. PRESENT CONTRIBUTIONS

From the open literature, it is clear that for $10^4 < Re_D < 10^7$ three distinct flow regimes are encountered:

- *subcritical*—laminar boundary layer separation upstream of 90°, followed by transition in the wake;
- *critical*—a separation bubble due to laminar separation, followed by transition away from the surface, followed by reattachment and a subsequent turbulent separation;
- *supercritical*—attached boundary layer transition upstream of 90°, followed by turbulent boundary layer separation at 115–120°.

There are several unresolved issues regarding computational prediction of the CCF:

- the qualitative ability of turbulence modelling to resolve boundary layer transition and separation for flow over a blunt body and to reproduce the three regimes described above for the CCF;
- the quantitative ability to predict separation angle and drag coefficient for this range of Re_D;
- the documentation of the sensitivity of the drag coefficient to the location of separation.

To address these issues, a series of 2-D unsteady simulations was performed. Results compare the performance of conventional, fully turbulent eddy–viscosity models (RKE and SKE) to a newly developed eddy–viscosity model that is capable of resolving laminar-to-turbulent boundary layer transition without *a priori* transition prescription or *ad hoc*, problem-dependent modifications and 'empirical' fixes.

3. COMPUTATIONAL METHODOLOGY

3.1. Computational model

Since the maximum Mach number of the flow was less than 0.1 and there was no energy transfer as work or heat, a constant temperature, density, and viscosity were employed. The set of governing equations solved for this flow consisted of continuity, mean momentum, and the turbulence model transport equations.

For this problem, separation and transition occur as unsteady, 2-D phenomena, and it is only in the downstream wake dynamics that three-dimensionality effects are observed to be significant. Especially at the largest Reynolds numbers, a full 3-D unsteady approach would be prohibitive. The 2-D model allows accurate resolution of the three distinct flow regimes, and is sufficient to demonstrate the role of boundary layer transition and separation on the flow physics. The relative importance of 3-D and unsteadiness depends on the flow regime.

For example, 3-D and unsteady effects are more significant for subcritical flow, and the 2-D simplification is expected to lead to some quantitative discrepancy with regard to the drag coefficient [11].

3.2. Geometry, grid, and boundary conditions

Though the current set of simulations is compared to several different experiments, a single geometry was used for all Reynolds numbers, and it is shown in Figure 1. Note the axis orientation and that θ is measured clockwise from the leading stagnation point. Certain criteria were met for the geometry. It was desired to have a minimal blockage effect from upper and lower boundaries, which was achieved with periodic boundaries at $\pm 8.5D$. The location of the upstream and downstream boundaries were placed far from the cylinder to not influence the flow ($6.5D$ upstream for the inlet and $10.5D$ downstream for the outlet). To show that the placement of the boundaries was adequate, additional simulations using a geometry twice as large as that used in the current study (inlet at $x = -12.5D$, outlet at $x = 18.5D$, and periodic boundaries at $y = \pm 18.5D$) were performed. Results were similar to those obtained with the smaller domain.

For the study of flow over a smooth cylinder with low mainstream turbulence, Re_D is the key dimensionless parameter. To vary Re_D, the dynamic viscosity (μ) was changed and all other quantities were held constant. The inlet boundary conditions were specified for a mainstream velocity (U_∞) of 15.345 m/s, a mainstream turbulent length scale (Lu) of $0.1D$, and a mainstream turbulence level (Tu) of 0.2%. A zero streamwise gradient was used at the outlet for static pressure and turbulence parameters.

The viscous sublayer was fully resolved in all simulations. To accomplish this, it was necessary to place at least 5 cells within $y^+ < 7$ in the near-wall region and to have $y^+ = 1$ for the first cell. Since the behaviour of the boundary layer and the location of separation are known to be a function of the Reynolds number, it was most efficient to make a different background mesh for each Re_D. In regions of separation, it is desirable to have cells with aspect ratios near unity to reduce the effects of numerical viscosity. A simple approach would be to fill the domain with equilateral triangles with a characteristic size of $y^+ = 1$. This would be computationally expensive for higher Re_D. Cells far away from the cylinder wall can be larger than cells near the wall. Also, if the direction of the flow is known, cells can have large aspect ratios as long as they are parallel to the flow direction, as in the boundary layer. Using these concepts, a reasonably sized and high-quality grid was obtained, and grid-independence was established by adding additional cells in regions of large changes in flow parameters with no appreciable change in the results [22]. For all cases, the background mesh was shown to be sufficiently fine to yield grid-independent results.

Experimental separation angle results and the concepts described above were used to customize the background grid as much as possible. For example, in supercritical flow, the boundary layer should transition upstream of 90° and separate around 120°. Therefore from 0 to 97°, a boundary layer type grid was employed. From 97 to 132°, the near-wall grid was modified to account for separation. Aspect ratios were reduced since the direction of the flow near the wall is not known *a priori* in a region of separated flow. A large band that encompassed the experimental separation point was used to ensure that high aspect ratio cells did not affect the results. Figure 2 shows the grid for $Re_D = 10^7$. Table I summarizes mesh sizes for each Re_D.

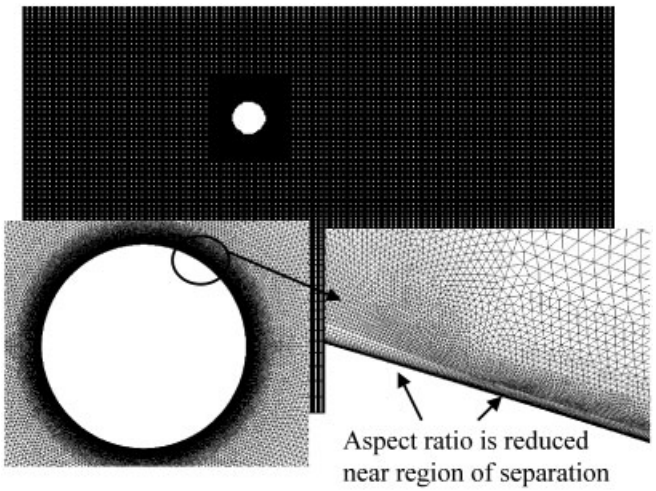

Figure 2. Multi-topology, multi-block grid for the supercritical flow case. Separation occurs at approximately 120°. This is the region where cells of lowest aspect ratio are concentrated.

Table I. Details of the grid for each flow regime.

Flow regime	Re_D	Total cells	Cells along cylinder	Aspect ratio in separation region
Subcritical	$10^4, 10^5$	213 K, 93 K	2100, 530	1, 10
Critical	10^6	323 K	6940	10
Supercritical	10^7	413 K	7031	10

3.3. Discretization scheme and solution method

All solutions were obtained with the second-order linear reconstruction discretization scheme used in conjunction with the segregated-implicit solver in Fluent 6. The new transition-sensitive turbulence model was implemented using the user-defined function capability. More details are given in Reference [23] and below. By using the second-order scheme and the hanging node adaptive tool in Fluent 6, the effects of numerical viscosity were minimized. The time step (independent of Re_D) was determined using a Strouhal number of 0.2, a velocity scale equal to the inlet velocity and a length scale equal to the diameter to find an estimated shedding period (T). A time step of $0.05T$ was used to ensure full time-resolution of the flowfield. This time step was deemed adequate since additional simulations using a time step of $0.025T$ showed no appreciable change in results.

In a steady framework, convergence implies that the solution does not change with additional iterations. This can be extended to an unsteady framework [22] by ensuring that the solution at each time step is fully converged and that time-averaged flow parameters do not change with additional time steps. The convergence within an individual time step is achieved by using an appropriate combination of time step size and number of iterations per time step. In all cases, 10 iterations per time step were adequate. Simulations were run on a cluster of

four SUN Ultra 60 workstations (each with 2 CPUs and 2 GB of RAM) connected with a gigabit switch and fibre-optic network at 15–60 s per time step depending on Re_D. Typically, 2000 time steps were required to converge the time-averaged quantities of key flow variables. Since the flow was treated as unsteady, simulations typically required more than an order of magnitude more clock time than their steady counterparts.

3.4. Turbulence modelling

The effects of transition in the current simulations are included using a newly developed, transition-sensitive turbulence model. This model has been previously documented [23–25] and is described below. Proper resolution of the effects of transition proved to be essential for a cylinder-in-crossflow over a wide range of Reynolds numbers. To accurately assess the performance of the new model and the importance of resolving boundary layer transition, comparison simulations were performed assuming fully laminar flow and fully turbulent flow using well-known models already in Fluent. It is known that a laminar simulation is inappropriate at high Reynolds numbers ($Re_D > 10^4$) and that fully turbulent models (RKE and SKE) are inappropriate at low Reynolds numbers ($Re_D < 3.5\times10^6$), and the results documented below confirm this.

3.4.1. New turbulence model equations. The concept and development of the new modelling approach has been documented in detail by the current authors [23] and will not be repeated here. This section presents the final model equations used in the present study. Differences between this model form and that in Reference [23] are discussed. The model form used herein is identical to that presented in two previously documented studies [24, 25].

The new model is a three-equation eddy–viscosity type, including transport equations for turbulent kinetic energy (k_T), laminar kinetic energy (k_L), and inverse turbulent time scale (ω):

$$\frac{Dk_T}{Dt} = P_{k_T} + R + R_{NAT} - \varepsilon - D_T + \frac{\partial}{\partial x_j}\left[\left(\nu + \frac{\alpha_T}{\sigma_k}\right)\frac{\partial k_T}{\partial x_j}\right] \tag{1}$$

$$\frac{Dk_L}{Dt} = P_{k_L} - R - R_{NAT} - D_L + \frac{\partial}{\partial x_j}\left[\nu\frac{\partial k_T}{\partial x_j}\right] \tag{2}$$

$$\frac{D\omega}{Dt} = P_\omega + C_{\omega R}\frac{\omega}{k_T}(R + R_{NAT}) - C_{\omega 2}\omega^2 + C_{\omega 3} f_\omega \alpha_T \left(\frac{\lambda_{eff}}{\lambda_T}\right)^{4/3} \frac{\sqrt{k_T}}{d^3} + \frac{\partial}{\partial x_j}\left[\left(\nu + \frac{\alpha_T}{\sigma_\omega}\right)\frac{\partial \omega}{\partial x_j}\right] \tag{3}$$

The laminar kinetic energy, k_L, represents the magnitude of non-turbulent streamwise fluctuations in the pre-transitional boundary layer, following the recommendation of Mayle and Schulz [26]. Note that the original model [23] used the turbulence farfield dissipation rate, ε, as the turbulence scale-determining variable. Use of the inverse turbulent time scale leads to a better representation of the breakdown of laminar kinetic energy to turbulence. The scalar

farfield turbulent dissipation rate is simply obtained as

$$\varepsilon = \omega k_{\mathrm{T}} \tag{4}$$

The influence of turbulent and laminar fluctuations on the mean flow is included through prescription of a total eddy viscosity

$$-\overline{u_i u_j} = \nu_{\mathrm{TOT}}\left(\frac{\partial U_i}{\partial x_j} + \frac{\partial U_j}{\partial x_i}\right) - \frac{2}{3} k_{\mathrm{TOT}} \delta_{ij} \tag{5}$$

The effective length scale and turbulence length scale are defined as

$$\lambda_{\mathrm{eff}} = \mathrm{MIN}(C_\lambda d, \lambda_{\mathrm{T}}) \tag{6}$$

$$\lambda_{\mathrm{T}} = k^{1.5}/\varepsilon \tag{7}$$

where d is the distance to the closest wall. Small- and large-scale energies are then calculated assuming the Kolmogorov inertial range spectrum applies over all wavenumbers greater than $1/\lambda_{\mathrm{T}}$:

$$k_{\mathrm{T,s}} = k_{\mathrm{T}}\left(\frac{\lambda_{\mathrm{eff}}}{\lambda_{\mathrm{T}}}\right)^{2/3} \tag{8}$$

$$k_{\mathrm{T},\ell} = k_{\mathrm{T}}\left[1 - \left(\frac{\lambda_{\mathrm{eff}}}{\lambda_{\mathrm{T}}}\right)^{2/3}\right] \tag{9}$$

The sum of (8) and (9) is the turbulent kinetic energy, k_{T}.

The first term on the right-hand side of Equation (1) is the production of turbulence by turbulent fluctuations and mean strain rate

$$P_{k_{\mathrm{T}}} = \nu_{\mathrm{T,s}} S^2 \tag{10}$$

The small-scale turbulent viscosity $\nu_{\mathrm{T,s}}$ is defined as

$$\nu_{\mathrm{T,s}} = \mathrm{MIN}\left(f_v f_{\mathrm{INT}} C_\mu \sqrt{k_{\mathrm{T,s}}}\lambda_{\mathrm{eff}}, \frac{2.5\varepsilon_{\mathrm{TOT}}}{S^2}\right) \tag{11}$$

The limit on turbulent viscosity is imposed to prevent too rapid production in the case of boundary layer separation and in highly strained freestream regions. Other terms in the definition of turbulent viscosity are

$$C_\mu = \frac{1}{A_0 + A_{\mathrm{s}}\left(\frac{Sk_{\mathrm{T}}}{\varepsilon}\right)} \tag{12}$$

$$f_v = 1 - \exp\left(-\frac{\sqrt{Re_{\mathrm{T,s}}}}{A_v}\right) \tag{13}$$

$$f_{\mathrm{INT}} = \mathrm{MIN}\left(\frac{k_{\mathrm{L}}}{C_{\mathrm{INT}}\, k_{\mathrm{TOT}}}, 1\right) \tag{14}$$

$$Re_{\mathrm{T,s}} = \frac{k_{\mathrm{T,s}}^2}{\nu\varepsilon} \tag{15}$$

Equation (14) defines a damping function on turbulent production due to intermittency, and is a modification to the original model [23]. This term helps to prevent over-prediction of momentum and scalar transport in the latter stages of bypass transition, which occurred with the original model.

The first term on the right-hand side of Equation (2) is the production of laminar kinetic energy by large-scale turbulent fluctuations

$$P_{k_{\mathrm{L}}} = \nu_{\mathrm{T},\ell} S^2 \tag{16}$$

The large-scale turbulent viscosity $\nu_{\mathrm{T},\ell}$ is modelled as

$$\nu_{\mathrm{T},\ell} = \mathrm{MIN}\left(\nu^*_{\mathrm{T},\ell}, \frac{0.5 k_{\mathrm{T},\ell}}{S}\right) \tag{17}$$

where

$$\nu^*_{\mathrm{T},\ell} = f_{\tau,\ell} C_{\ell 1}\left(\frac{\Omega\lambda_{\mathrm{eff}}^2}{\nu}\right)\sqrt{k_{\mathrm{T},\ell}}\lambda_{\mathrm{eff}} + \beta_{\mathrm{TS}} C_{\ell 2}\phi_{\mathrm{NAT}}\, \mathrm{d}^2\Omega \tag{18}$$

The limit introduced in Equation (17) ensures that realizability is not violated in the developing pre-transitional boundary layer. The time-scale-based damping function $f_{\tau,\ell}$ is

$$f_{\tau,\ell} = 1 - \exp\left[-C_{\tau,\ell}\left(\frac{\tau_{\mathrm{m}}}{\tau_{\mathrm{T},\ell}}\right)^2\right] \tag{19}$$

$$\tau_{\mathrm{T},\ell} = \lambda_{\mathrm{eff}}/\sqrt{k_{\mathrm{T},\ell}} \tag{20}$$

$$\tau_{\mathrm{m}} = 1/\Omega \tag{21}$$

The second term on the right-hand side of Equation (18) includes the following:

$$\beta_{\mathrm{TS}} = 1 - \exp\left(-\frac{\mathrm{MAX}(\phi_{\mathrm{NAT}} - C_{\mathrm{TS,crit}}, 0)^2}{A_{\mathrm{TS}}}\right) \tag{22}$$

$$\phi_{\mathrm{NAT}} = \mathrm{d}^2\Omega/\nu \tag{23}$$

Near-wall dissipation is given by

$$D_{\mathrm{T}} = 2\nu \frac{\partial\sqrt{k_{\mathrm{T}}}}{\partial x_j}\frac{\partial\sqrt{k_{\mathrm{T}}}}{\partial x_j} \tag{24}$$

$$D_{\mathrm{L}} = 2\nu \frac{\partial\sqrt{k_{\mathrm{L}}}}{\partial x_j} \frac{\partial\sqrt{k_{\mathrm{L}}}}{\partial x_j} \tag{25}$$

and the total dissipation rate of fluctuation energy, $\varepsilon_{\mathrm{TOT}}$, is defined as

$$\varepsilon_{\mathrm{TOT}} = \varepsilon + D_{\mathrm{T}} + D_{\mathrm{L}} \tag{26}$$

The term R that appears in Equations (1)–(3) represents the averaged effect of the breakdown of streamwise fluctuations into turbulence during bypass transition, and has been modified from [23] to

$$R = C_{\mathrm{R}} \beta_{\mathrm{BP}} k_{\mathrm{L}} \omega \left(\frac{\lambda_{\mathrm{T}}}{\lambda_{\mathrm{eff}}} \right)^{2/3} \tag{27}$$

The threshold function β_{BP} controls the bypass transition process

$$\beta_{\mathrm{BP}} = 1 - \exp\left(-\frac{\phi_{\mathrm{BP}}}{A_{\mathrm{BP}}} \right) \tag{28}$$

$$\phi_{\mathrm{BP}} = \mathrm{MAX}\left[\left(\frac{\sqrt{k_{\mathrm{T}}} d}{\nu} - C_{\mathrm{BP,\,crit}} \right), 0 \right] \tag{29}$$

The breakdown to turbulence due to instabilities is included as a separate natural transition 'production' term:

$$R_{\mathrm{NAT}} = C_{\mathrm{R,\,NAT}} \beta_{\mathrm{NAT}} k_{\mathrm{L}} \Omega \tag{30}$$

$$\beta_{\mathrm{NAT}} = 1 - \exp\left[-\frac{\mathrm{MAX}(\phi_{\mathrm{NAT}}^{0.75} \phi_{\mathrm{MIX}}^{0.25} - C_{\mathrm{NAT,\,crit}}, 0)}{A_{\mathrm{NAT}}} \right] \tag{31}$$

$$\phi_{\mathrm{MIX}} = \sqrt{k_{\mathrm{L}}}\, \mathrm{d}/\nu \tag{32}$$

The coefficient $C_{\omega R}$ in Equation (3) enforces a reduction of turbulent length scale during the transition breakdown, and takes the functional form

$$C_{\omega R} = 1.5 \left(\frac{\lambda_{\mathrm{T}}}{\lambda_{\mathrm{eff}}} \right)^{2/3} - 1 \tag{33}$$

The first term on the right-hand side of Equation (3) is the increase in inverse turbulent time scale due to either turbulence production mechanisms or flowfield instabilities. It takes the form

$$P_\omega = (C_{\omega\ell} \nu_{\mathrm{T},\,\omega} S^2 + f_{\Delta P} C_{\Delta P} k_{\mathrm{T},\,\ell} \Omega) \frac{\omega}{k_{\mathrm{T}}} \tag{34}$$

The first term inside the parenthesis is due to turbulent production, where the effective turbulent viscosity corresponds to that in Equation (11) without any imposed limit:

$$\nu_{\mathrm{T},\omega} = f_\nu f_{\mathrm{INT}} C_\mu \sqrt{k_{\mathrm{T,\,s}}} \lambda_{\mathrm{eff}} \tag{35}$$

The second term represents the increase in inverse turbulent time scale in unstable regions of the boundary layer subjected to an adverse pressure gradient. The damping function $f_{\Delta P}$ is a function of the gradient of the magnitude of the rotation rate tensor in the wall-normal direction, and it takes the form

$$\begin{aligned} f_{\Delta P} &= f_{\tau,\ell} \quad \text{if } \partial\Omega/\partial d > 0 \\ f_{\Delta P} &= 0 \qquad \text{if } \partial\Omega/\partial d \leqslant 0 \end{aligned} \tag{36}$$

In Equation (3), the coefficient $C_{\omega 2}$ is assigned the following functional form:

$$C_{\omega 2} = 0.92\left(\frac{\lambda_{\text{eff}}}{\lambda_{\text{T}}}\right)^{4/3} \tag{37}$$

This form enforces a decrease in the turbulent length scale close to the wall.

The use of ω as the scale-determining variable can lead to a reduced intermittency effect in the outer region of a turbulent boundary layer, and consequently an elimination of the wake region in the velocity profile. The third term on the right-hand side of Equation (3) is included to rectify this. The term includes the following damping function:

$$f_\omega = 1 - \exp\lfloor -0.41(\lambda_{\text{eff}}/\lambda_{\text{T}})^4 \rfloor \tag{38}$$

The total eddy–viscosity in Equation (5) is given by

$$\nu_{\text{TOT}} = \nu_{\text{T,s}} + \nu_{\text{T},\ell} \tag{39}$$

Finally, the turbulent scalar diffusivity in Equations (1) and (3) is given by

$$\alpha_{\text{T}} = f_v C_{\mu,\text{std}} \sqrt{k_{\text{T}}}\lambda_{\text{eff}} \tag{40}$$

The inlet boundary conditions for k_{T} and ω are set as for any two-equation model to reproduce the desired turbulence intensity and scale. Since the computational inlet is located in the freestream, far from any solid boundary, k_{L} is set to zero. At solid walls, all three model equations use zero-flux boundary conditions:

$$\frac{\partial k_{\text{T}}}{\partial \eta} = 0 \tag{41}$$

$$\frac{\partial k_{\text{L}}}{\partial \eta} = 0 \tag{42}$$

$$\frac{\partial \omega}{\partial \eta} = 0 \tag{43}$$

To evaluate the gradient terms at the wall in Equations (24) and (25), the wall values of $\sqrt{k_{\text{T}}}$ and $\sqrt{k_{\text{L}}}$ are taken to be zero. This is done independent from the boundary condition for k_{T} and k_{L}. The above model equations and boundary conditions yield the correct asymptotic behaviour at solid boundaries, i.e. $k \sim d^2$ and $\varepsilon_{\text{TOT}} \to 2\nu k/d^2$ as $d \to 0$.

The model constants are summarized in Table II. These constants were determined based on comparison with direct numerical simulations of fully turbulent channel flow [27] and

Table II. Summary of model constants for the new transition-sensitive eddy–viscosity turbulence model.

$A_0 = 4.04$	$A_s = 2.12$	$A_v = 6.75$	$A_{BP} = 3$
$A_{NAT} = 60$	$A_{TS} = 200$	$C_{BP,crit} = 12$	$C_{NAT,crit} = 440$
$C_{INT} = 0.75$	$C_{TS,crit} = 1000$	$C_{R,NAT} = 0.04$	$C_{\ell 1} = 3.4\times10^{-6}$
$C_{\ell 2} = 1.0\times10^{-9}$	$C_R = 0.08$	$C_{\alpha,\theta} = 0.035$	$C_{\tau,\ell} = 4360$
$C_{\omega 1} = 0.44$	$C_{\Delta P} = 0.15$	$C_{\omega 3} = 0.3$	$C_\lambda = 2.495$
$C_{\mu,std} = 0.09$	$\mathrm{Pr}_\theta = 0.85$	$\sigma_k = 1$	$\sigma_\omega = 1.17$

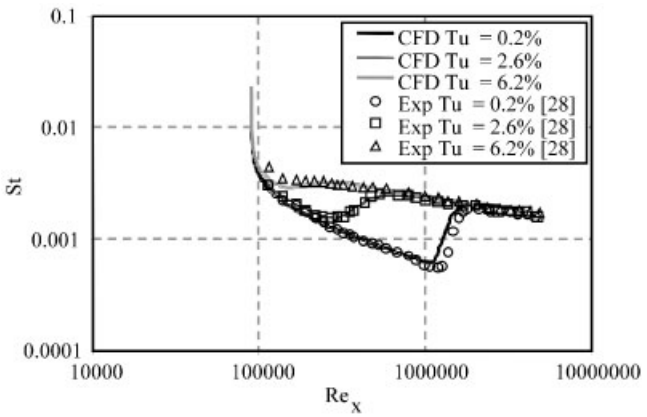

Figure 3. Stanton number distribution for flat plate test case, highlighting the ability of the new turbulence model to resolve boundary layer transition over a range of freestream turbulence intensities [23].

flat-plate boundary layer experiments [28]. Note that some constants have been modified from the original version of the model [23]. Figure 3 shows the heat transfer distribution on a flat plate boundary layer, using the current version of the turbulence model. Results are compared to an experimental test case [28] and the details of the numerical method are documented in Reference [23]. The figure demonstrates the ability of the new model to resolve transition over a range of freestream turbulence intensities for this simple but crucial reference case.

3.4.2. Reference turbulence models. The performance of fully turbulent eddy viscosity models for this problem is documented using two reference models: standard k–ε (SKE), and the realizable k–ε (RKE) model proposed by Shih *et al.* [29]. Both models are implemented with the two-layer near-wall treatment of Wolfstein [30]. The models are eddy–viscosity type, with two transport equations in the outer layer for turbulent kinetic energy, k_T, and turbulent dissipation rate, ε_{TOT}, and a single transport equation for k_T and an algebraic prescription for dissipation rate and length scale in the near-wall inner layer. Both models, considered 'industry standards', are available in most commercial CFD codes—including Fluent—and have been used in numerous CFD studies documented in the open literature. Readers are referred to References [29–31] for a complete description.

4. RESULTS AND DISCUSSION

The results of this study are presented in two sections. First, simulations with the new model are compared to laminar and fully turbulent simulations to highlight the ability of the new model to resolve transition. The next section examines quantitative prediction of separation angle and drag coefficient, including the role of transition, and compares results to available experimental data.

4.1. Comparison of turbulence models

The major contribution of the new turbulence model is its ability to perform in laminar, transitional, and turbulent flows. This is imperative for accurate resolution of separated flow over a blunt body. To assess the performance of the model for the CCF, comparisons are made at Reynolds numbers that best highlight the contrasts between the fully turbulent models and the new model. For the cases under consideration, the standard and realizable forms of the fully turbulent k–ε model produced similar results.

At a Reynolds number of 10^6 (critical regime), the flow physics are complex. The laminar boundary layer separates downstream of 90°, transitions to turbulence in the separated shear layer, reattaches, and separates again downstream of 120°. Figures 4 and 5 show a comparison between the new model and RKE. Figure 4 is a plot of normalized, time-averaged turbulent kinetic energy, k_T, for the first cell grid centre along the top half of the cylinder. Comparing the results shows that the RKE model reproduces a turbulent boundary layer from the stagnation point ($\theta = 0°$) onward, whereas the new model is laminar until approximately $\theta = 105°$. The plot indicates that the new model is capable of capturing transition to turbulence, whereas RKE is not.

To ascertain if the model can capture the separation, transition, reattachment, and second separation phenomenon at $Re_D = 10^6$, the normalized, time-averaged streamwise velocity, U, is plotted for the first cell grid centre along the top half of the cylinder in Figure 5. A

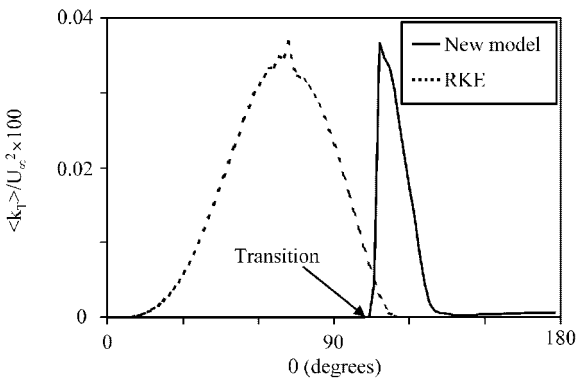

Figure 4. Profiles of normalized, time-averaged k_T along the top of the cylinder (results are symmetric for bottom half of cylinder) for RKE and in-house model at a critical $Re_D = 10^6$. Fully turbulent models are incapable of resolving the laminar-to-turbulent transition that is known to occur at this Reynolds number.

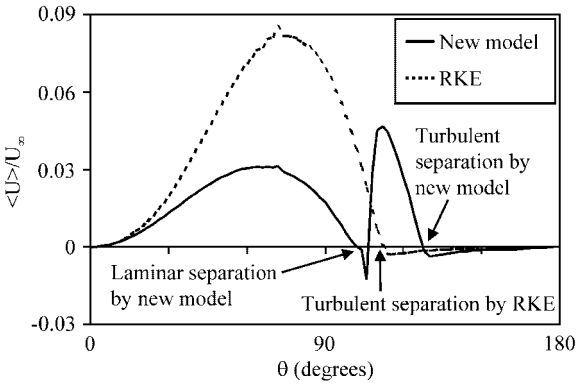

Figure 5. Profiles of normalized, time-averaged U along the top of the cylinder for RKE and in-house model at a critical $Re_D = 10^6$. The new model captures a laminar separation followed by a turbulent separation while the RKE model captures only one turbulent separation.

separation region is indicated by a negative value of $\langle U \rangle$, and separation or reattachment occurs where $\langle U \rangle = 0$. For the RKE model, the boundary layer is turbulent starting at $\theta = 0°$ and separates at approximately 112°. This is a typical result for all Reynolds numbers when using a fully turbulent model form. However, using the new model, the flow is predicted to separate (laminar separation) at $\theta = 103°$, transition at approximately 105°, reattach at 107°, and separate again (turbulent separation) at 127°. Recall that in Reference [5] measurements at a similar Reynolds number of 8.5×10^5 showed the existence of the separation bubble with an initial laminar separation at 105°. To our knowledge this is the first time in the open literature that this complex phenomenon has been captured using CFD with an eddy–viscosity, RANS-based turbulence model. The key lies in the ability of the new model to resolve the transitional behaviour, which in turn strongly influences the boundary layer separation and reattachment physics for flow over a blunt body.

Figure 6 shows $\langle U \rangle / U_\infty$ along the top half of the cylinder for subcritical ($Re_D = 10^5$) and supercritical ($Re_D = 10^7$) flows, comparing the results using the new model and the RKE model. It is apparent that the RKE model predicts only one characteristic flow regime regardless of Reynolds number, which is a fully turbulent boundary layer that separates between 111° and 120°. The flow behaviour is that of supercritical flow regardless of the Reynolds number. The fact that a fully turbulent model form is inappropriate for subcritical (and critical) flow regimes is certainly not a surprise, but it does highlight the importance of resolving boundary layer transition. In contrast to RKE, the new model predicts three distinct regimes, depending on Reynolds number. For subcritical flow, separation occurs at 75°. For supercritical flow, separation occurs at 119°, and the results downstream of 70° are similar to those from the RKE model. This is expected since the new model should behave like a fully turbulent model as Re_D increases and the boundary layer becomes turbulent over the majority of the cylinder surface.

Figure 7 shows normalized $\langle k_T \rangle$ along the top half of the cylinder for subcritical ($Re_D = 10^5$) and supercritical ($Re_D = 10^7$) flows, comparing the results using the new model and the RKE model. The behaviour highlighted above is apparent. The RKE model predicts a turbulent

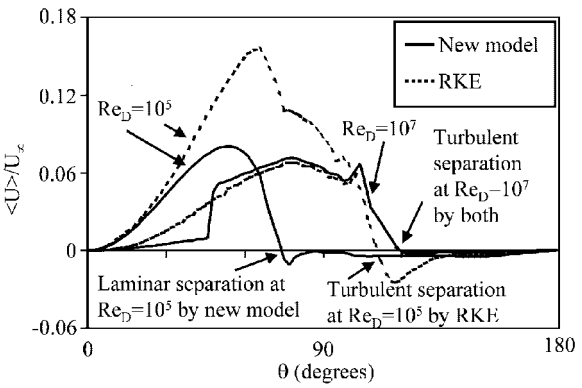

Figure 6. Profiles of normalized, time-averaged U along the top of the cylinder for RKE and the new model at a subcritical $Re_D = 10^5$ and supercritical $Re_D = 10^7$. The in-house model captures a laminar separation for subcritical flow at 75° and a turbulent separation for supercritical flow at 119°. RKE predicts a turbulent separation between 111 and 120° regardless of Re_D.

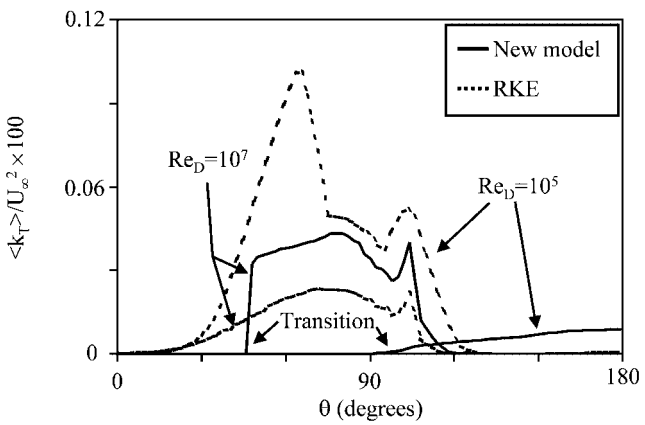

Figure 7. Profiles of normalized, time-averaged k_T along the top of the cylinder for RKE and in-house model at a subcritical $Re_D = 10^5$ and supercritical $Re_D = 10^7$. The new model predicts transition for the subcritical flow at 98° and the supercritical flow at 47°.

boundary layer over the entire cylinder surface, whereas the new model shows Reynolds-number-sensitive transitional effects. For subcritical flow, the new model shows transition to occur at 98°, which is downstream of the predicted separation. For supercritical flow, the new model predicts transition at 47°. Both results correspond qualitatively to experimental values documented in the open literature.

Figure 8 shows the transitional effects more visually using contour plots of $\langle k_T \rangle$ and $\langle U \rangle$ for $Re_D = 10^5$ through 10^7. The view is a close-up of the top half of the cylinder. At the subcritical Reynolds number, the flow transitions away from the surface after it has separated. At the critical $Re_D = 10^6$, the separation, transition, reattachment, and second separation phenomenon

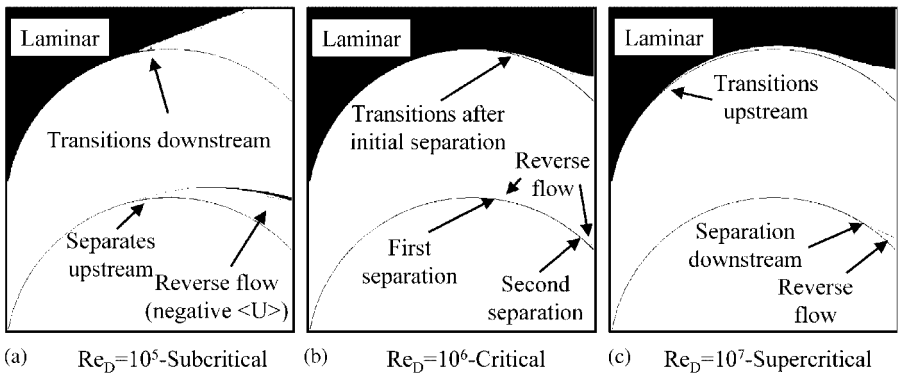

Figure 8. Contours of $\langle k_T \rangle$ and $\langle U \rangle$ along the top of the cylinder for the in-house model for (a) subcritical (b) critical and (c) supercritical flows. For the $\langle k_T \rangle$ contours (top), the black region indicates negligible turbulence. For $\langle U \rangle$ (bottom), non-white indicates reversed flow.

is apparent. Finally, the supercritical flow regime is correctly resolved as shown with boundary layer transition and a single subsequent turbulent separation. At $Re_D = 10^7$, similar results are obtained for the fully turbulent models and the new model.

4.2. Comparisons with experiments

While the above section highlights the performance of the new model in a qualitative sense, this section compares numerical and experimental values of drag coefficient (C_D) and separation angle (θ_s). The importance of capturing transition will be highlighted again. Drag and separation angle must be considered together due to the strong functional dependence of C_D on θ_s. It will be shown that an extreme sensitivity to separation location is the primary reason that accurate drag prediction for blunt bodies is difficult using CFD.

Figure 9 shows a plot of time-averaged C_D as a function of Re_D for both computations and experiments [1]. The drag coefficient data is taken from the time average of fluctuating quantities, such as in Figure 10. These results are from computations using the new, transition model. Similar levels of oscillations were found using RKE. As can be seen, C_D for the high Reynolds number case (10^6) changes very little in time. Similar results are obtained for 10^7. This nearly steady behaviour at high Re_D was also seen in Reference [13] for URANS calculations. However, LES results from Reference [13] showed a more significant oscillation in C_D at $Re_D = 10^6$. This implies that traditional, steady-based turbulence models need improvement to be used in a wide variety of unsteady flows. At lower Reynolds numbers, there are signs of time dependence in the drag coefficient data, as in Reference [16]. However, the results at $Re_D = 10^6$ imply that the level of unsteadiness at $Re_D = 10^4$ may also be under-predicted using traditional URANS.

Examining the time-averaged drag coefficient results in Figure 9 shows that the new model, which includes the effects of laminar-to-turbulent transition, is the only turbulence treatment that successfully captures the well-known drag crisis. This is shown with high values of C_D (≈ 1) for subcritical flow followed by a sudden drop in C_D (≈ 0.15) in the critical

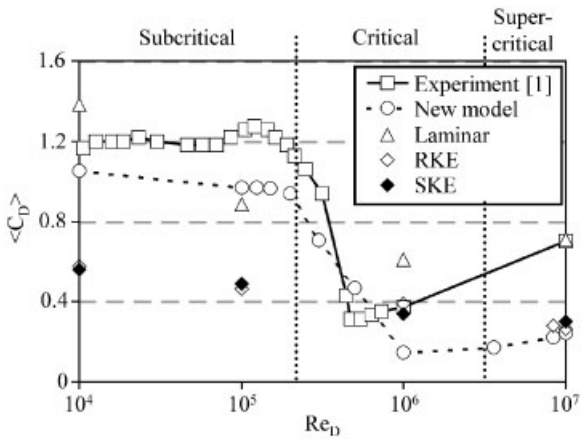

Figure 9. Time-averaged drag coefficient as a function of Re_D. The new model (which includes effects of laminar-to-turbulent transition) is the only model that captures the correct trend in drag with increasing Re_D. However, the magnitudes do not agree with the experimental values, particularly at high Re_D.

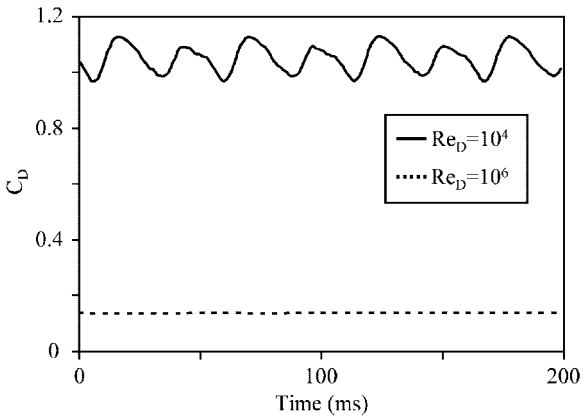

Figure 10. Variation of drag coefficient with time for low and high Reynolds numbers from CFD results using the new, in-house turbulence model. Simulations using URANS show very little unsteadiness at high Reynolds number. Similar levels of oscillations were found using RKE.

range. Finally, there is an increase in C_D to 0.25 at the supercritical Re_D. While the new model reproduces the correct physical behaviour, including the drag crisis, the predicted drag coefficients do not agree well overall with the experimental data. It should be pointed out there is a large scatter in the experimental data for critical and supercritical flow. For example in Reference [32], the drag coefficient is reported as 0.2 for $Re_D \approx 10^6$ and 0.53 for $Re_D \approx 8\times10^6$. The reference turbulence models (SKE and RKE) show an interesting and inaccurate trend. As Re_D increases, the drag coefficient asymptotically decreases to a value of approximately 0.3 at the supercritical Reynolds number. As with the new model, C_D for the supercritical regime differs significantly from the measured result.

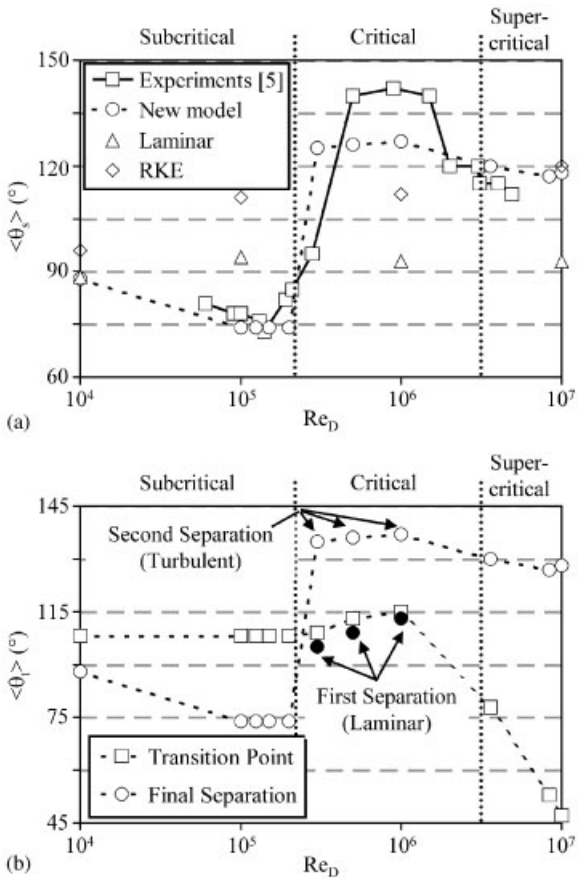

Figure 11. Time-averaged (a) separation angle as a function of Re_D for computations and experiments and (b) transition location and separation angle for simulations using the new, transition model.

Figure 11(a) shows a plot of time-averaged separation angle as a function of Reynolds numbers for both experiments [5] and computations. For critical flow, this data represents the location of the second, turbulent separation. It should be noted that only the in-house model predicts a change in separation angle with a change in Reynolds number. Figure 11(b) shows the predicted location of transition when using the new, in-house model. Included in this plot is the separation angle data from Figure 11(a) and the location of the first separation (laminar) point for critical flow. Recall that this is the only turbulence treatment that predicts transition for all Reynolds numbers and the separation bubble for critical flow. Examining the results for each flow regime in Figure 11(b) again shows the characteristics seen in Figures 4–8 and reported in References [1, 5].

As expected, the C_D and θ_s results using the new model approach those obtained from the fully turbulent models in the supercritical regime. In the subcritical and critical regimes, however, considerable difference is noted. The values for RKE and SKE in these regimes are

obtained from time-averaging results that do not match the separation and transition physics seen in experiments. This was shown in the section above and is expected since fully turbulent models should only work well for almost fully turbulent flows (supercritical). Likewise, the laminar results at the higher Reynolds numbers are obtained from time-averaging a physically incorrect flowfield. Interestingly, at the highest Reynolds number, the laminar result shows the best agreement with the measured value of C_D. This contradictory result underscores the difficulty in predicting the CCF, and indicates that proper resolution of separation and transition effects is not the only issue facing CFD.

The separation angle data in Figure 11(a) help to clarify some of the results seen in Figure 9. The total drag on the cylinder is comprised of a pressure part (form drag) and a viscous part (skin drag). At high Re_D, the drag over a blunt object is dominated by form drag, which primarily depends on the separation location. As θ_s increases, it is expected that the form and total drag will decrease. The sudden increase in separation angle is the cause of the drag crisis. Figure 11(a) shows that the separation angle is predicted relatively well by the new model for all flow regimes. Possible reasons for the lack of agreement in drag coefficient, despite relatively good prediction of the separation angle, are discussed for each regime in the following paragraphs.

In the subcritical and critical regimes, the near-field downstream region is dominated by quasi-periodic unsteady and three-dimensional flow, more so than at a supercritical Reynolds number. The fact that the simulations in the present study are 2-D may explain much of the discrepancy in C_D [11], even when using the transition-sensitive turbulence model. However, there is good prediction of the separation angle, which suggests that using the new modelling approach with fully 3-D, unsteady computations may lead to much improved predictive capability in these regimes. Efforts are underway that address the ability to properly capture unsteady and turbulent flows, including 3-D URANS using both currently available turbulence models and new models that contain more unsteady physics.

For the supercritical regime, the effects of unsteadiness and three-dimensionality are expected to be less important than for subcritical flows [1]. Though the simulations with the new model show that drag coefficient increases between $Re_D = 10^6$ and 10^7, there is a significant discrepancy between the experimental value of 0.7 and the computed value of 0.25. Likewise, the values for the fully turbulent models are 0.26 for RKE and 0.3 for SKE; as discussed above, similar results are expected between all three models in this regime. Figure 11(a) shows that all three turbulence models yield a separation point at approximately 120° whereas the experiments show values ranging from 115° to 120°. The range in the experiments is a result of measurement uncertainty as well as variations of mainstream turbulence, surface characteristics, etc. At first glance, it appears that the CFD prediction of separation angle is quite good. It is therefore surprising that the drag coefficient is so significantly underpredicted. An explanation for this can be obtained by examining the static pressure distribution at $Re_D = 3.6\times10^6$ as shown in Figure 12. The experimental data of Achenbach [5] is compared with two computational plots, where one is the actual result that shows a separation at 118° and the other is identical to the actual CFD result up to the experimental separation point of 116°. At this point, it is assumed that separation occurs and that the static pressure remains constant along the cylinder surface in the wake region. The purpose of this plot is to investigate the relative change in predicted form drag due to the relatively small, yet constant, over-prediction of the separation angle. For this Reynolds number, the skin drag is two orders of magnitude less than the form drag.

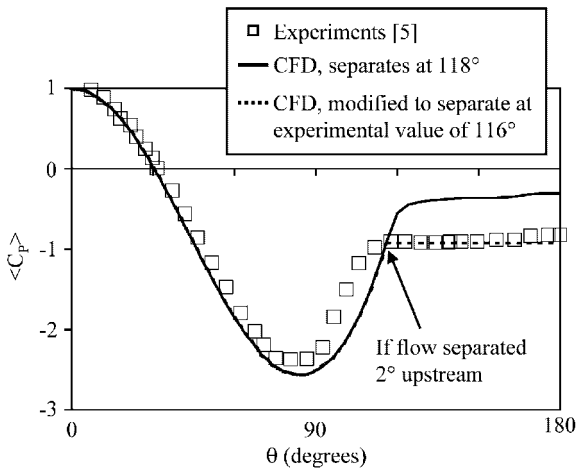

Figure 12. Profiles of time-averaged pressure coefficient along the top of the cylinder for experiments and the new model at a supercritical $Re_D = 3.6\times10^6$. Two curves are used for the CFD: the actual result that shows a separation at 118°; the other is identical up to the experimental separation at 116°. This plot shows the importance of resolving the separation point exactly for supercritical flow over a blunt body.

By using symmetry and Equation (44) to integrate around the circumference of the cylinder, the time-averaged pressure drag coefficient for the three curves can be obtained

$$\langle C_{D,p}\rangle = \int_0^{\pi} \langle C_P\rangle \cos\theta \, d\theta \tag{44}$$

A comparison of the experimental, the actual CFD, and the modified CFD values of $C_{D,p}$ shows 0.84, 0.23, and 0.72, respectively. The modified CFD value, though only based on a 2° difference in separation angle, is dramatically different from the actual CFD result, and leads to a much better agreement with experiments. Though the modification is rather *ad hoc*, it shows the significance of capturing the separation point exactly. The error in the C_D is mostly due to this over-prediction in separation angle since it is in this region that the form drag is determined. The form drag is sensitive to the separation angle in this region because of the large pressure gradient—a small change in separation angle leads to a large change in the pressure at the separation point. The fact that the separation angle is consistently over-predicted in the supercritical regime for all of the eddy–viscosity based models implies that there may be an inherent reason that the turbulent boundary layer is predicted to remain attached too far downstream. One possible explanation is the inability of the models used in the present study to predict the effects of curvature on turbulence. However, the use of a differential Reynolds stress model that could account for the effects of streamline curvature would still lack the ability to predict the important effects of transition. It should be noted that for flows over streamlined bodies such as airfoils, where skin drag is a more important contribution to overall drag and in which the streamwise pressure gradients are often less steep in the separation region, a slight over-prediction in the separation location will likely yield

only a small change in overall drag. For these cases, it is the ability to capture transition itself that will aid significantly in the prediction of heat transfer and wall shear stress. This has been recently demonstrated for turbine airfoil profile loss and conjugate heat transfer predictions [33, 34].

5. CONCLUSIONS

The importance of being able to predict transition in RANS-based CFD for flow over blunt bodies was demonstrated by examining a circular cylinder-in-crossflow for subcritical, critical, and supercritical flow ($Re_D = 10^4$–10^7). Computations compared the performance of fully turbulent eddy–viscosity models (RKE and SKE) to a newly developed model that is capable of capturing the laminar-to-turbulent transition in a hands-off, physics-based manner. Details of the model were given, and it was shown, as expected, that the inclusion of transition effects was necessary to capture the correct trends for this flow. These trends include the drag crisis that occurs in the critical flow regime ($Re_D > 1.3\times10^5$) and the ability to produce characteristics of three distinct flow regimes. These characteristics are summarized below:

- *subcritical*—laminar separation upstream of 90°, followed by transition to turbulence in the wake;
- *critical*—laminar separation, followed by transition in the separated shear layer, followed by reattachment and a subsequent turbulent separation;
- *supercritical*—laminar-to-turbulent transition of the attached boundary layer, with the location depending on Re_D, followed by separation at approximately 119°.

To the authors' knowledge, this is the first time in the open literature that a RANS-based simulation has been shown to correctly predict these distinct flow regimes.

It was also shown that despite proper resolution of the flow physics and qualitative trends, discrepancies still exist between the magnitudes of experimental and computational results. At subcritical and critical Reynolds numbers, the physics of the interaction between the unsteadiness and turbulence in the wake and the three-dimensionality of flowfield are not resolved in the simulations, and are believed to contribute to the differences. For supercritical flows, the effects of unsteadiness and three-dimensionality are less important. However, there are consistently large discrepancies for C_D between the experimental values and all of the computational results, which is most likely due to the fact that the predicted boundary layer separation is a few degrees downstream of the measured data. This slight difference in separation angle makes a dramatic difference in predicted form and overall drag due to the large streamwise pressure gradient typical of blunt bodies in this region. For streamlined bodies, where total drag is mostly due to skin drag, predictive capability using the new model is expected to be much less sensitive to this effect, and has in fact been shown [33, 34].

NOMENCLATURE

$\langle A \rangle$ time-average of quantity A
CCF cylinder-in-crossflow

C_D coefficient of drag, $F_D/(0.5\rho U_{in}^2 D)$
$C_{D,p}$ coefficient of form drag, $F_{D,p}/(0.5\rho U_{in}^2 D)$
C_p coefficient of pressure, $(P - P_{in})/(0.5\rho U_{in}^2)$
C_μ turbulent viscosity coefficient
D cylinder diameter (m)
D_L laminar kinetic energy near-wall dissipation (m^2/s^3)
D_T turbulent kinetic energy near-wall dissipation (m^2/s^3)
d wall distance (m)
F_D total drag force (N)
f_v viscous damping function
f_{INT} intermittency damping function
$f_{\tau,\ell}$ time-scale damping function
f_{BP} bypass transition parameter
f_{NAT} natural transition parameter
k_T turbulent kinetic energy (m^2/s^2)
k_L non-turbulent kinetic energy (m^2/s^2)
k total fluctuation kinetic energy ($k_T + k_L$) (m^2/s^2)
L cylinder length (m)
Lu integral length scale (m)
P static pressure (Pa)
P_L laminar kinetic energy production term (m^2/s^3)
P_T turbulent kinetic energy production term (m^2/s^3)
P_ω 'production' term governing increase in inverse turbulent time scale ($1/s^2$)
R bypass transition production term (m^2/s^3)
R_{NAT} natural transition production term (m^2/s^3)
Re_D Reynolds number based on diameter, $U_{in}D/v$
Re_T turbulence Reynolds number
S magnitude of mean strain rate tensor, $\sqrt{2S_{ij}S_{ij}}$
S_{ij} strain rate tensor, $0.5((\partial U_i/\partial x_j) + (\partial U_j/\partial x_i))$
T shedding period (s)
TL turbulence level, $\sqrt{\frac{2}{3}k_t}/U_{in}$
U x-direction (streamwise) velocity (m/s)
$-\overline{u_i u_j}$ kinematic Reynolds stress tensor (m^2/s^2)
u_τ wall friction velocity (m/s)
y^+ non-dimensional wall distance, du_τ/v
α_T turbulent diffusivity for turbulent quantities (m^2/s)
β_{BP} bypass transition threshold function
β_{TS} Tollmien–Schlichting threshold function
β_{NAT} natural transition threshold function
ε farfield turbulent dissipation rate (m^2/s^3)
η local wall-normal coordinate direction
λ_{eff} effective (wall-limited) length scale (m)
λ_T turbulent length scale (m)
μ dynamic viscosity (Ns/m^2)
v kinematic viscosity (m^2/s)
v_T turbulent kinematic viscosity (m^2/s)

ν_{TOT}	total (laminar + turbulent) eddy viscosity (m^2/s)
θ_s	separation angle ($^\circ$)
θ_t	transition location ($^\circ$)
ρ	density (kg/m^3)
Ω	magnitude of mean rotation tensor, $\sqrt{2\Omega_{ij}\Omega_{ij}}$
Ω_{ij}	rotation rate tensor, $0.5((\partial U_i/\partial x_j) - (\partial U_j/\partial x_i))$
ω	inverse turbulent time scale, ε/k_T
τ_m	mean flow time scale
τ_T	turbulent time scale

Subscripts

i, j	indices
ℓ	large scale
s	small scale
in	inlet value

ACKNOWLEDGEMENTS

The authors would like to thank Fluent, Inc. for their continued support with special thanks to Rick Lounsbury and Evangelos Koutsavdis. Special thanks also to Will Robinson and Jabbar Stackston, Clemson University College of Engineering and Science Computer & Network Services, for excellent support of computing systems.

REFERENCES

1. Schlichting H, Klaus G. *Boundary Layer Theory*. Springer: New York, 2000.
2. Bloor MS. The transition to turbulence in the wake of a circular cylinder. *Journal of Fluid Mechanics* 1963; **19**(2):290–304.
3. Humphreys JS. On a circular cylinder in a steady wind at transition Reynolds numbers. *Journal of Fluid Mechanics* 1960; **9**(4):603–612.
4. Zdravkovich MM. Conceptual overview of laminar and turbulent flows past smooth and circular cylinders. *Journal of Wind Engineering and Industrial Aerodynamics* 1990; **33**:53–62.
5. Achenbach E. Distribution of local pressure around a circular cylinder in cross-flow up to $Re = 5\times10^6$. *Journal of Fluid Mechanics* 1968; **34**(4):625–639.
6. Farell C, Blessman J. On critical flow around smooth circular cylinders. *Journal of Fluid Mechanics* 1983; **136**:375–391.
7. Roshko A. Experiments on flow past a circular cylinder at very high Reynolds number. *Journal of Fluid Mechanics* 1961; **10**(2):345–356.
8. Breuer M. A challenging test case for large eddy simulation: high Reynolds number circular cylinder flow. *International Journal of Heat and Fluid Flow* 2000; **21**:648–654.
9. Cantwell B, Coles D. An experimental study on entrainment and transport in the turbulent near wake of a circular cylinder. *Journal of Fluid Mechanics* 1983; **136**:321–374.
10. Selvam RP. Finite element modelling of flow around a circular cylinder using LES. *Journal of Wind Engineering and Industrial Aerodynamics* 1997; **67&68**:129–139.
11. Tamura T, Ohta I, Kuwahara K. On the reliability of two-dimensional simulation for unsteady flows around a cylinder-type structure. *Journal of Wind Engineering and Industrial Aerodynamics* 1990; **35**:275–298.
12. Reichel C, Strohmeier K. Calculation of incompressible flow around a circular cylinder. *American Society of Mechanical Engineers, Pressure Vessels and Piping Division (Publication) PVP* 2002; **446**(2):43–50.
13. Catalano P, Wang M, Iaccarino G, Moin P. Numerical simulation of the flow around a circular cylinder at high Reynolds numbers. *International Journal of Heat and Fluid Flow* 2003; **24**:463–469.
14. Celik I, Shaffer FD. Long time-averaged solutions of turbulent flow past a circular cylinder. *Journal of Wind Engineering and Industrial Aerodynamics* 1995; **56**:185–212.

15. Travin A, Shur M, Strelets M, Spalart P. Detach-eddy simulations past a circular cylinder. *Flow, Turbulence and Combustion* 2000; **63**:293–313.
16. Saghafian M, Stansby PK, Saidi MS, Apsley DD. Simulation of turbulent flows around a circular cylinder using nonlinear eddy–viscosity modeling: steady and oscillatory ambient flows. *Journal of Fluids and Structures* 2003; **17**(8):1213–1236.
17. Craft TJ, Launder BE, Suga K. Development and application of a cubic eddy–viscosity model of turbulence. *International Journal of Heat and Fluid Flow* 1996; **17**(2):108–115.
18. Edwards JR, Roy CJ, Blottner FG, Hassan HA. Development of a one-equation transition/turbulence model. *AIAA Journal* 2001; **39**(9):1691–1698.
19. Spalart PR, Allmaras SR. A one-equation turbulence model for aerodynamics flow. *AIAA Paper No*. 92-0439, 1992.
20. Warren ES, Hassan HA. Transition closure model for predicting transition onset. *Journal of Aircraft* 1998; **35**(5):769–775.
21. Warren ES, Hassan HA. An alternative to the e^n method for determining the onset of transition. *AIAA Paper No*. 97-0825, 1997.
22. Holloway DS, Walters DK, Leylek JH. A practical perturbation-based unsteady CFD methodology. *AIAA Paper No.* ISABE-2003-1214, 2003.
23. Walters DK, Leylek JH. A new model for boundary layer transition using a single-point RANS approach. *ASME Journal of Turbomachinery* 2004; **126**(1):193–202.
24. Walters DK, Leylek JH. Simulation of transitional boundary layer development on a highly-loaded turbine cascade with advanced RANS modeling. *ASME IGTI Paper* GT2003-38664, 2003.
25. Walters DK, Leylek JH. A CFD study of wake-induced transition on a compressor-like flat plate. *ASME IGTI Paper* GT2003-38680, 2003.
26. Mayle RE, Schulz A. The path to predicting bypass transition. *ASME Journal of Turbomachinery* 1997; **119**: 405–411.
27. Kim J, Moin P, Moser, RD. Turbulence statistics in fully developed channel flow at low Reynolds number. *Journal of Fluid Mechanics* 1987; **177**:133–186.
28. Blair MF. Influence of free-stream turbulence on turbulent boundary layer heat transfer and mean profile development, part I—experimental data. *ASME Journal of Heat Transfer* 1983; **105**:33–40.
29. Shih T-H, Liou WW, Shabbir A, Yang Z, Zhu J. A new k–ε eddy–viscosity model for high Reynolds number turbulent flows. *Computers & Fluids* 1995; **24**:227–238.
30. Wolfstein M. The velocity and temperature distribution of one-dimensional flow with augmentation and pressure gradient. *International Journal of Heat and Mass Transfer* 1969; **12**:201–318.
31. Fluent User's Manual Version 6.0. 2001.
32. Schewe G. On the force fluctuations acting on a circular cylinder in crossflow from subcritical up to transcritical Reynolds numbers. *Journal of Fluid Mechanics* 1983; **133**:265–285.
33. Walters DK, Leylek JH. Prediction of boundary layer transition effects on turbine airfoil profile losses. *ASME Paper* IMECE2003-41420, 2003.
34. York WD, Walters DK, Leylek JH. A novel transition-sensitive conjugate methodology applied to turbine vane heat transfer. *ASME Paper* IMECE2003-41555, 2003. *ASME Journal of Turbomachinery* (in press).

